

Supporting information

Coating Dynamics in Two-Step Hybrid Evaporated/Blade-Coated Perovskites for Scalable Fully-Textured Perovskite/Silicon Tandem Solar Cells

Oussama Er-raji^{1,2}, Ahmed A. Said³, Anand S. Subbiah³, Vladyslav Hnapovskiy³, Badri Vishal³, Anil R. Pininti³, Marco Marengo³, Martin Bivour¹, Markus Kohlstädt^{1,4}, Juliane Borchert^{1,2}, Patricia S. C. Schulze¹, Stefaan De Wolf³, Stefan W. Glunz^{1,2}*

¹Fraunhofer Institute for Solar Energy Systems ISE, Heidenhofstr. 2, 79110 Freiburg, Germany

²Chair of Photovoltaic Energy Conversion, Department of Sustainable Systems Engineering (INATECH), University of Freiburg, Emmy-Noether-Strasse 2, 79110 Freiburg, Germany

³Center for Renewable Energy and Storage Technologies (CREST), Physical Sciences and Engineering, Division (PSE), King Abdullah University of Science and Technology (KAUST), Thuwal 23955-6900, Kingdom of Saudi Arabia

*Email: oussama.er-raji@ise.fraunhofer.de

Experimental section

Silicon heterojunction bottom-cell fabrication: The fabrication of silicon bottom cells began with approximately 250 μm thick *p*-type float-zone silicon wafers (Siltronic), featuring a base resistivity of 1 $\Omega\text{ cm}$. An industrial double-sided random pyramid texture was created using an aqueous KOH solution (SINGULUS SILEX), resulting in pyramid sizes ranging from 1 to 4 μm on both sides. The wafers were then subjected to ozone-based wet chemical cleaning before being transferred to a plasma-enhanced chemical vapor deposition (PECVD) cluster tool (INDEOtec Octopus II). On both sides of the wafers, a passivation stack of intrinsic and doped hydrogenated amorphous silicon (a-Si:H) layers was deposited. The layer thicknesses were set to approximately 12 nm for the *p*-doped and *n*-doped layers, and 6 nm for the intrinsic layer. The parallel-plate PECVD reactor was operated at 13.56 MHz and 200 $^{\circ}\text{C}$, using gas mixtures of SiH_4 , H_2 , PH_3 , and trimethylboron for the deposition processes. Subsequently, a recombination layer was formed on the front side of the silicon via a 1 cm^2 shadow mask using direct current (DC) sputtered indium tin oxide (ITO, $\text{In}_2\text{O}_3/\text{SnO}_2 = 97/3$ wt%, VON ARDENNE SCALA in-line system) with a mixed oxygen/argon atmosphere. The rear contact was completed by sputtering 195 nm of ITO, followed by thermal evaporation of a 1000 nm silver layer covering the full area. Finally, the wafers were laser-scribed into 2.5×2.5 cm^2 substrates, with the 1×1 cm^2 ITO pad on the front side defining the active area.

Ohmic textured silicon substrate fabrication: Ohmic silicon substrates for single-junction perovskite solar cells were fabricated in a similar manner. These architectures are designed to provide equivalent substrate properties (Si morphology/texture and recombination TCO) as the bottom cell, ensuring similar top-cell growth conditions, while intentionally omitting the *p*-*n* junction. For this, *n*-type float-zone silicon wafers (1 $\Omega\text{ cm}$ base resistivity) were used instead of *p*-type wafers. On the rear side, the *p*-doped a-Si:H layer was replaced by *n*-doped a-Si:H. The rear TCO was omitted, and a Ti/Ag metal stack was deposited by thermal evaporation.

Perovskite top-cell fabrication: The silicon bottom cells were initially cleaned with ethanol (EtOH) using a dynamic spin-coating process (200 μL at 2500 rpm for 30 seconds) to remove any silicon particles from the laser scribing procedure. They were then treated with ultraviolet/ozone for 900 seconds to eliminate contaminants and activate the surface for the subsequent deposition of a self-assembled monolayer (SAM) as a hole transport layer. Next, the SAM was formed by statically spin-coating 100 μL of [4-(3,6-dimethyl-9H-carbazol-9-yl)butyl]phosphonic acid (Me-4PACz, from TCI or Dyenamo) dissolved in EtOH at a concentration of 1 mg/mL (with a 2-second waiting time, 800 rpm for 5 seconds, followed by 5000 rpm for 20 seconds). This was followed by post-annealing at 100 $^{\circ}\text{C}$ for 10 minutes and an EtOH washing step to remove any excess non-covalently bound Me-4PACz molecules, using the same spin-coating recipe as for Me-4PACz. Here, we note that while SAM was deposited via spin-coating, multiple reports demonstrated its scalable deposition via spray-coating, blade-coating, slot-die coating, and thermal evaporation.¹⁻⁷ The perovskite absorber was then deposited

using a hybrid evaporation/wet-chemical method. The evaporation step was carried out in an Ångström system with CsBr (from Abcr) and PbI₂ (from Alfa Aesar) as co-evaporation precursors set at ~ 460°C and ~ 380°C (rate-controlled sources) to reach 0.1 Å/s and 1 Å/s rates, respectively. Subsequently, either blade-coating or spin-coating was used as the second wet-chemical step. For blade-coating, a Zehntner ZAA 2300 setup was used, and the process parameters were varied as detailed in the Results and Discussion section. For single junction and tandem solar cells, the blade-coated solution consisted of FABr and FAI (from Dyenamo) with a volume ratio of FABr/FAI = 60/40 vol% and a concentration of 0.80M in addition to 4 mg/mL of urea as a crystallization agent (in comparison to our previous work no optimization of the concentration was done)⁸, dissolved in n-butanol. The use of urea is important to enhance the perovskite film properties as shown in Figure S17 of the Supporting Information. The blade-speed was set to 20 mm/s, the blade gap was set to 370 μm (250 μm in single-junction solar cells due to the change in silicon thickness, Figure S18), and the volume was set to 20 μL. The coating was carried-out at room temperature, without N₂-knife assistance. In spin-coating, the concentration of formamidinium halides was set to 0.72M (with no change in urea concentration) and the used solvent was ethanol. The spin-coating parameters were set to 2200 rpm spin-coating speed, 35s spin time and 150 μL solution volume. The final annealing treatment to complete the perovskite crystallization was conducted at 100°C for 10 minutes in air with a relative humidity of approximately 40-50%, enabling the formation of the perovskite with an estimated composition of FA_{0.78}Cs_{0.22}Pb(I_{0.77}Br_{0.23})₃ (from STEM-EDX). For top interface passivation, 1,3-diaminopropane dihydroiodide (PDAI) was deposited as described in this work.⁹ The substrates were transferred to the evaporation chamber, where an 18 nm thick C₆₀ layer was deposited at a rate of 0.1 Å/s. The SnO_x buffer layer was then deposited by atomic layer deposition (ALD), with a thickness of 15 nm using a Picosun tool. The substrate temperature was maintained at 80°C during the ALD process. The front transparent conductive oxide (TCO) contact was sputtered on top of the SnO_x layer through a shadow mask, with 55 nm of IZO using an Angstrom EvoVac tool. The top electrode was formed by evaporating 650 nm of silver (Ag) using a high-precision shadow mask at a deposition rate of approximately 3 Å/s. Finally, 140 nm of MgF_x was thermally evaporated as an antireflection layer at a deposition rate of approximately 2 Å/s. The evaporation rates and thicknesses of all evaporated layers were monitored and controlled using quartz-crystal microbalances, with the base evaporation pressure maintained below 3 × 10⁻⁶ mbar. The thickness of all evaporated layer is given for planar substrates. On textured substrates, the texture factor of 1.4 should be taken into account.

Tandem solar cell encapsulation: The encapsulation of the tandem solar cell involved tabbing the cell with PV ribbon and silver paste to establish the required electrical connections. Following this preparation, the encapsulation stack was assembled in the following sequence: a base layer of solar glass (70 × 70 mm, 3.2 mm thick) was placed at the bottom, over which a layer of thermoplastic polyurethane (TPU) encapsulant was laid. The tandem cell was positioned atop this TPU layer, followed by the application of a second TPU encapsulant layer. A top layer of solar glass, identical in dimensions to the

bottom layer, was then added to complete the stack. To protect the encapsulated cell from moisture penetration, an edge sealant composed of desiccated polyisobutylene (PIB) was applied along the edges of both glass sheets. The entire stack underwent processing in an industrial vacuum laminator (Ecolam 5, Ecoprogetti) at a temperature of 120°C for a duration of 20 minutes. This process ensured strong adhesion between the layers, resulting in a robust and stable encapsulation that effectively shields the cell from environmental degradation. A depiction of the encapsulated tandem cell is provided in Figure S19.

Characterization techniques

XRD: X-ray diffraction measurements were conducted using a Bruker D2 Phaser diffractometer (Cu-K α 1 radiation, $\lambda = 1.5406 \text{ \AA}$) within the 2θ range of 5° to 45°, with a step size of 0.03° and a time per step of 0.1 s. Data analysis was performed using DIFRAC.EVA software.

SEM: Cross-sectional scanning electron microscopy images were taken using a Carl Zeiss AURIGA CrossBeam workstation using an in-lens detector. The electron acceleration voltage was set to 5 kV and the working distance to nearly 6 mm.

Hyperspectral PL: The PL signal, with a spectral resolution of 2 nm, was obtained using a hyperspectral imaging system integrated with an optical microscope (Photon etc. IMA). To analyze the *QFLS*, also referred to as the iV_{OC} , a 532 nm wavelength laser was employed. The excitation power of the laser was carefully calibrated to replicate the photon flux absorbed by the sample under standard solar spectrum conditions (AM1.5G, 100 mW cm⁻²).¹⁰ A calibration procedure, thoroughly described in prior research,¹⁰ was applied to the collected signals to determine absolute values of emitted photon flux. The calibrated spectra were utilized to estimate *QFLS* at each pixel within an area of 300 μm by 300 μm . This estimation was carried out using the generalized Planck law, implemented via a custom MATLAB code¹⁰:

$$J \sim \alpha(E) \frac{E^2}{e^{\frac{E-\Delta\mu}{kT}} - 1}$$

Here, J represents the emitted photon flux density, $\alpha(E)$ is the absorption coefficient, $\Delta\mu$ is the Quasi-Fermi level splitting, E denotes photon energy, and kT corresponds to thermal energy.

PESA: photoemission spectroscopy in air was performed using a Riken AC2 setup. The schematic energy band diagram shown in Fig. S14 was constructed as follows: PESA measurements were used to determine the VBM and HOMO levels of the perovskite absorber, as well as those of the ITO substrates with and without Me-4PACz. To identify the CBM and the LUMO levels of both the perovskite and the modified ITO substrates, the optical bandgap of the materials—obtained from UV-vis measurements—was added to their respective CBM and LUMO levels. All measurements were carried out on textured silicon substrates.

GIWAXS: Grazing-incidence wide-angle X-ray scattering (GIWAXS) data are acquired using a Xenocs Xeuss 3.0 equipped with a Genix 3D Cu source with focused beam collimation, $l = 1.54 \text{ \AA}$, and an Eiger 2R 4M detector. The sample-to-detector distance was set to 150 mm, and the incidence angle was set to 1° . Each frame was acquired using an exposure of 360 s. Wedge correction and linecut integration were performed using XSACT by Xenocs.

STEM: A cross-sectional, electron-transparent TEM lamella was prepared using a focused ion beam (FIB)-equipped scanning electron microscope (SEM-FIB) Helios G4 DualBeam, FEI. Scanning Transmission Electron Microscopy (STEM)-based experiments were then conducted using a Cs probe-corrected ThermoFisher Titan 60-300 Cubed TEM microscope operating at 300 kV.

***jV* measurements:** *jV* measurements were performed using a WVELABS SINUS-220 light-emitting diode (LED)-based solar simulator was utilized. Spectrum calibration was performed using a Fraunhofer ISE-certified calibration cell, with no spectral mismatch factor applied. To control the illumination area of the devices, a laser-cut shadow mask with a 1.04 cm^2 opening was employed. Measurements were conducted within the voltage range of -100 mV to 2050 mV , at a scan speed of 200 mV/s , first in the reverse scan and then in the forward scan. Device characterization with *jV*, *EQE*, and reflection was performed in air, with a relative humidity of approximately 50–60%.

EQE: *EQE* measurements were carried out using a PV-Tools LOANA tool. For the perovskite top cell measurement, the tandem device was light-biased with infrared LEDs (930 nm), while the silicon bottom cell measurement was ensured by light-biasing the tandem solar cell with a blue LED (440 nm) to saturate the sub-cell. Note that the measured *EQEs* are not absolute.

Reflection: Reflection measurements were performed using a PV-Tools LOANA tool.

UV-vis: UV-vis measurements were performed to obtain reflectance (*R*) and transmittance (*T*) data. These measurements were conducted using a Lambda 950 spectrometer (PerkinElmer) over a wavelength range of 250-1200 nm, with a step size of 2 nm. The absorbance (*A*) was calculated using the formula $A = 1 - R - T$.

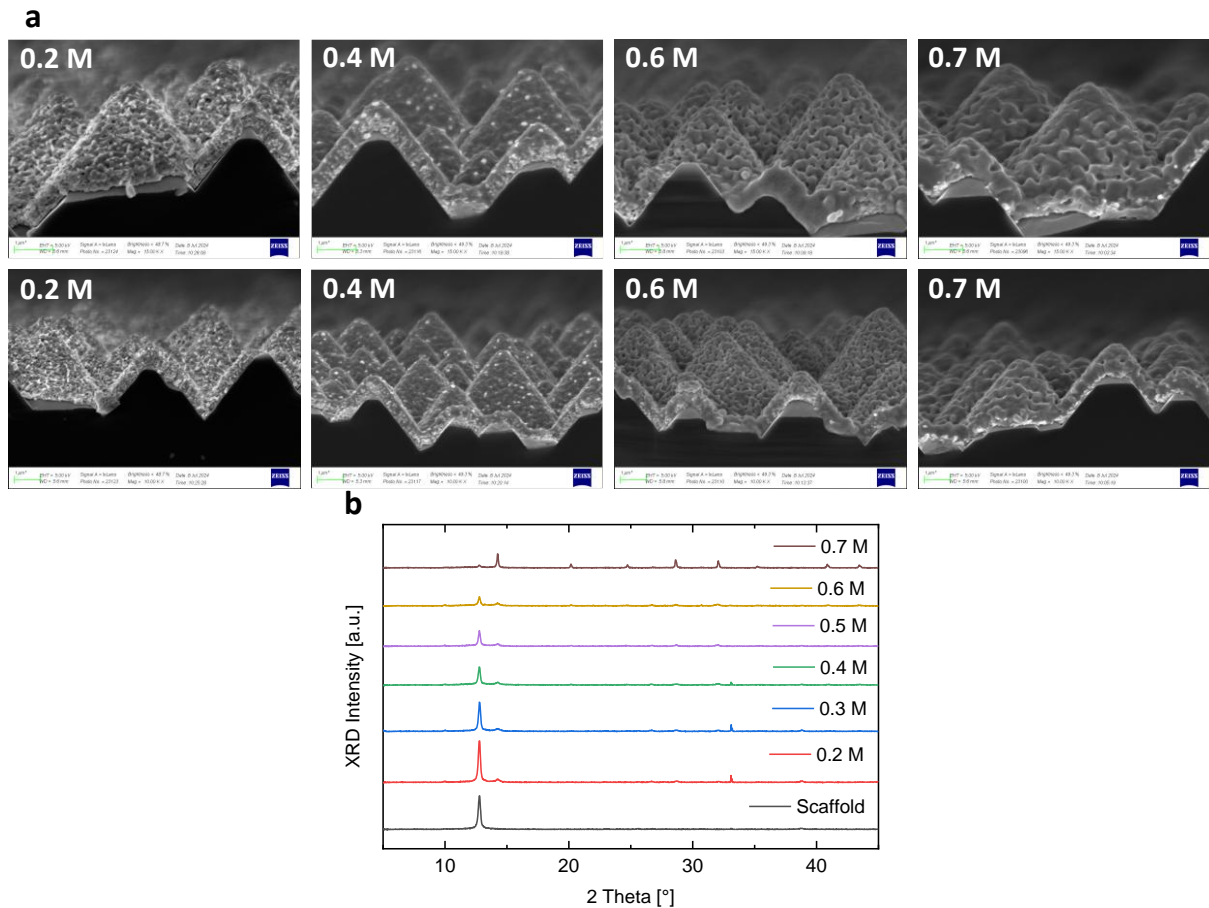


Figure S1. Impact of organohalide solution concentration (with ethanol as a solvent) on the perovskite's morphological and structural properties. (a) Cross-sectional SEM images, and (b) XRD data of perovskite films with a variation in organohalide solution concentration using ethanol. With increased solution concentration, the PbI₂ (100) peak intensity (at 12.69°) is reduced, and the perovskite's (001) main peak intensity is enhanced. However, the film's morphological property remains poor.

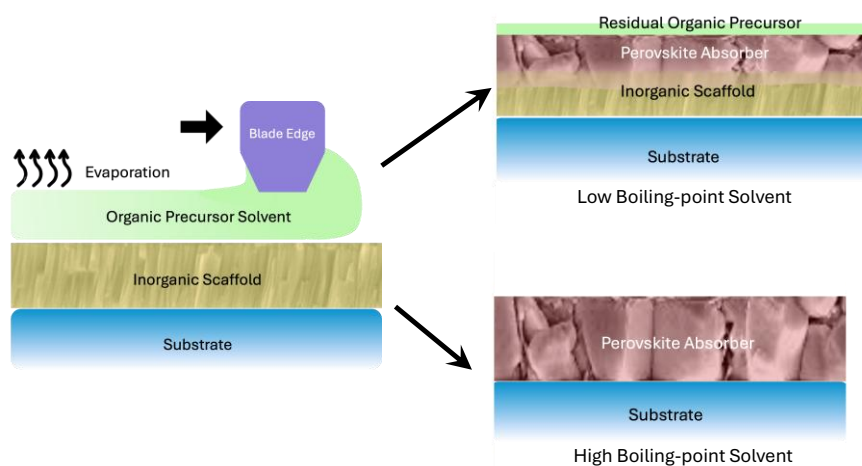


Figure S2. Schematic depicting the impact of boiling point on the conversion with the hybrid evaporation/blade-coating method. Low boiling point solvents evaporate quickly, resulting in organic precursor crystallization on the scaffold surface. Conversely, solvents with high boiling point result in a stable meniscus formation, extending the solution-scaffold interaction, and thus enabling a complete perovskite conversion.

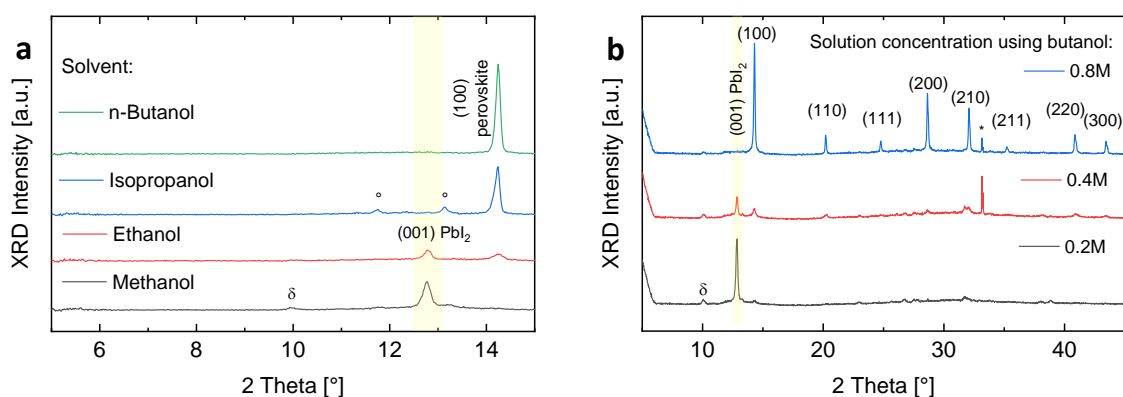


Figure S3. Impact of solvent and solution concentration using n-butanol. (a) Zoomed-in X-ray diffractograms of the XRD data shown in Fig. in of the main text (δ perovskite, \circ additional phases). (b) XRD data of perovskite films using n-butanol solvent with a variation in solution concentration (δ perovskite, * Si (002)). The organohalide solution concentration must be optimized to ensure full perovskite conversion.

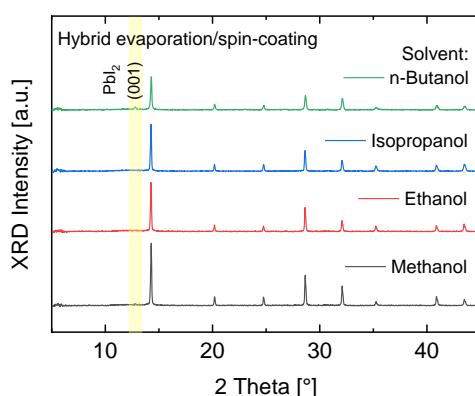


Figure S4. Impact of the solvent on perovskite films synthesized with the hybrid evaporation/spin-coating method. XRD data of perovskite films with a variation in solvent. With increased solvent boiling point (methanol to n-butanol), the perovskite crystallinity and the perovskite conversion rate are deteriorated (in contrast to observations in the hybrid evaporation/blade-coating method). We note that the impact of this variation could be more prominent if a solution with a lower concentration was used.

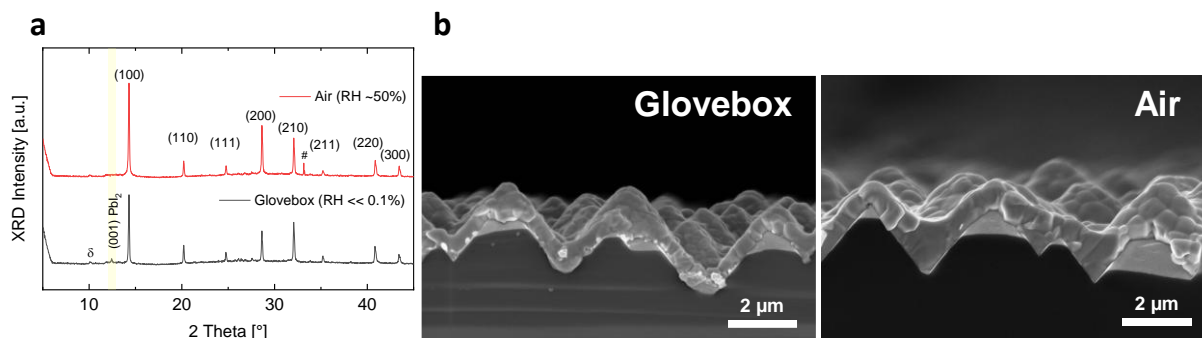


Figure S5: Impact of annealing environment on perovskite quality. (a) XRD data and (b) SEM cross-sectional images. Annealing in air is beneficial for perovskite crystallization with the hybrid evaporation/blade-coating method.

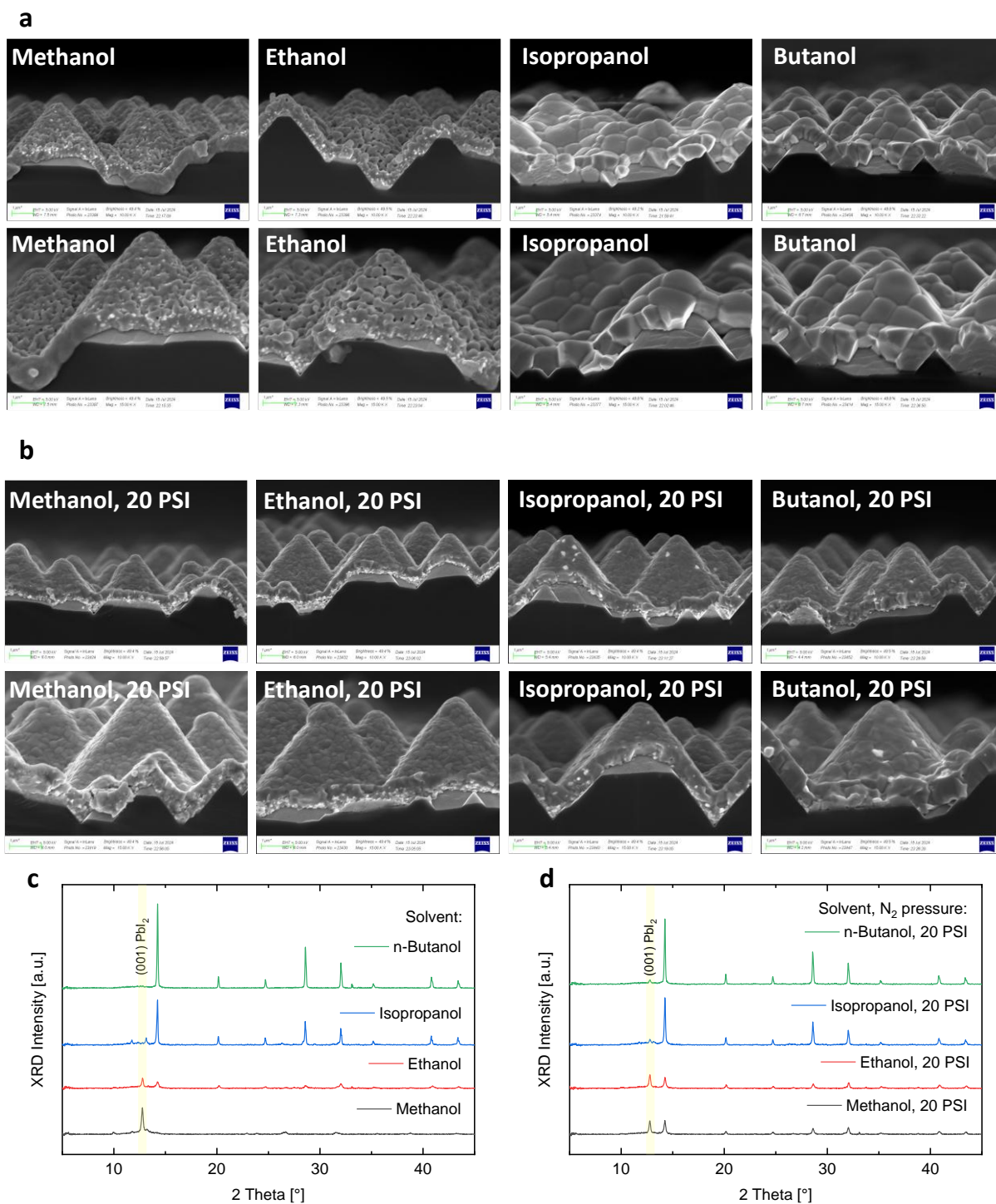


Figure S6. Impact of N₂-knife pressure on the perovskite's morphological and structural properties using different solvents. Cross-sectional SEM images of perovskite films synthesized with different solvents either (a) without N₂-knife or (b) with N₂-knife (20 PSI). XRD data of perovskite films synthesized with different solvents either (c) without N₂-knife or (d) with N₂-knife (20 PSI). While introducing pressure from an N₂-knife enhances the perovskite film compactness, it reduces the apparent grain size and deteriorates the perovskite conversion.

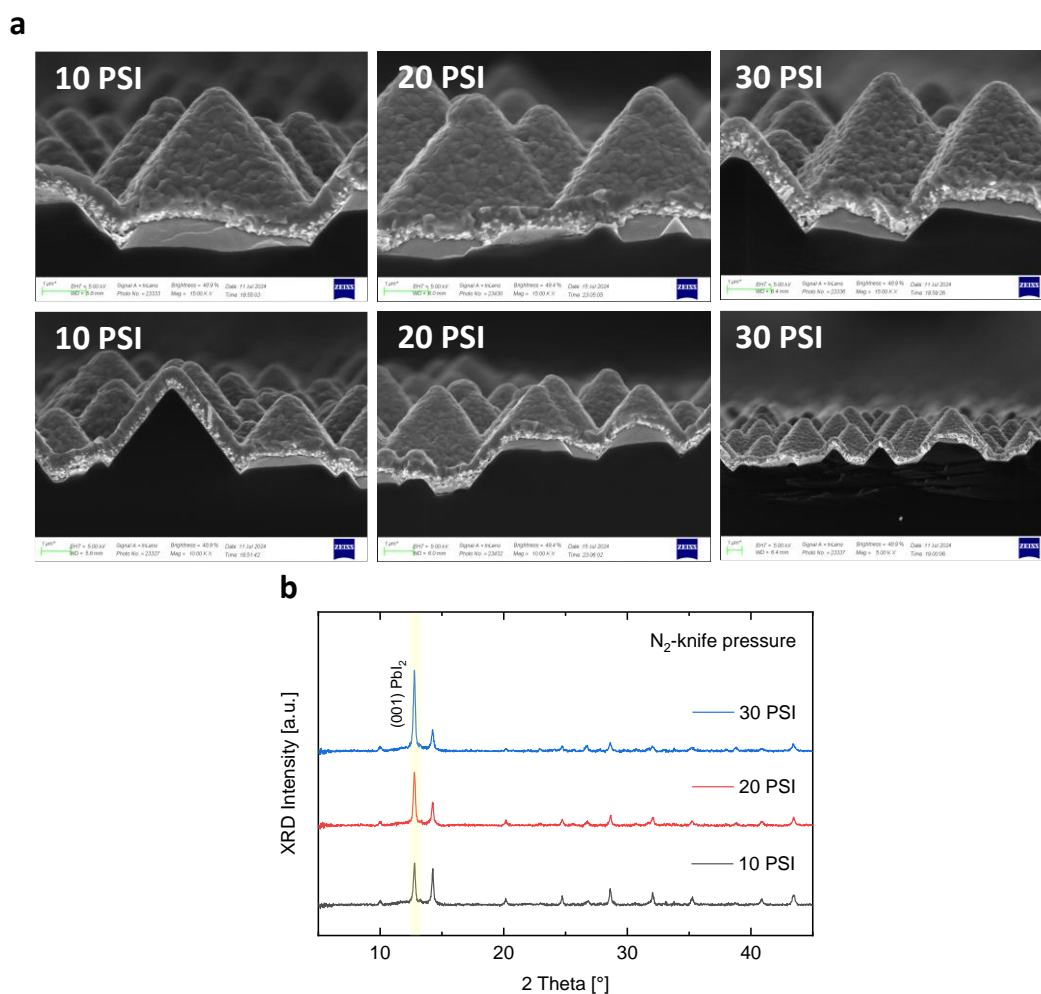


Figure S7. Impact of N_2 -knife pressure value on the perovskite's morphological and structural properties using ethanol as a solvent. (a) Cross-sectional SEM images and (b) XRD data of perovskite films with a variation in N_2 -knife pressure. With increased pressure value, the perovskite's crystallinity and conversion rate are deteriorated.

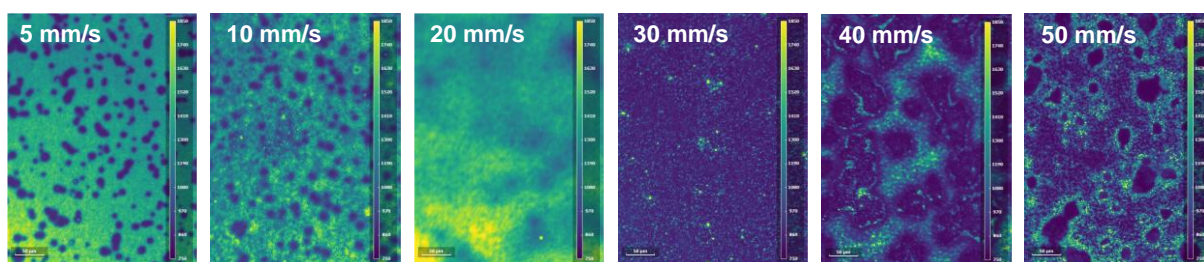


Figure S8. Impact of the coating speed on the perovskite's morphological and optoelectronic properties, assessed via hyperspectral PL. Beyond the optimum value of 20 mm/s, the PL intensity is significantly reduced.

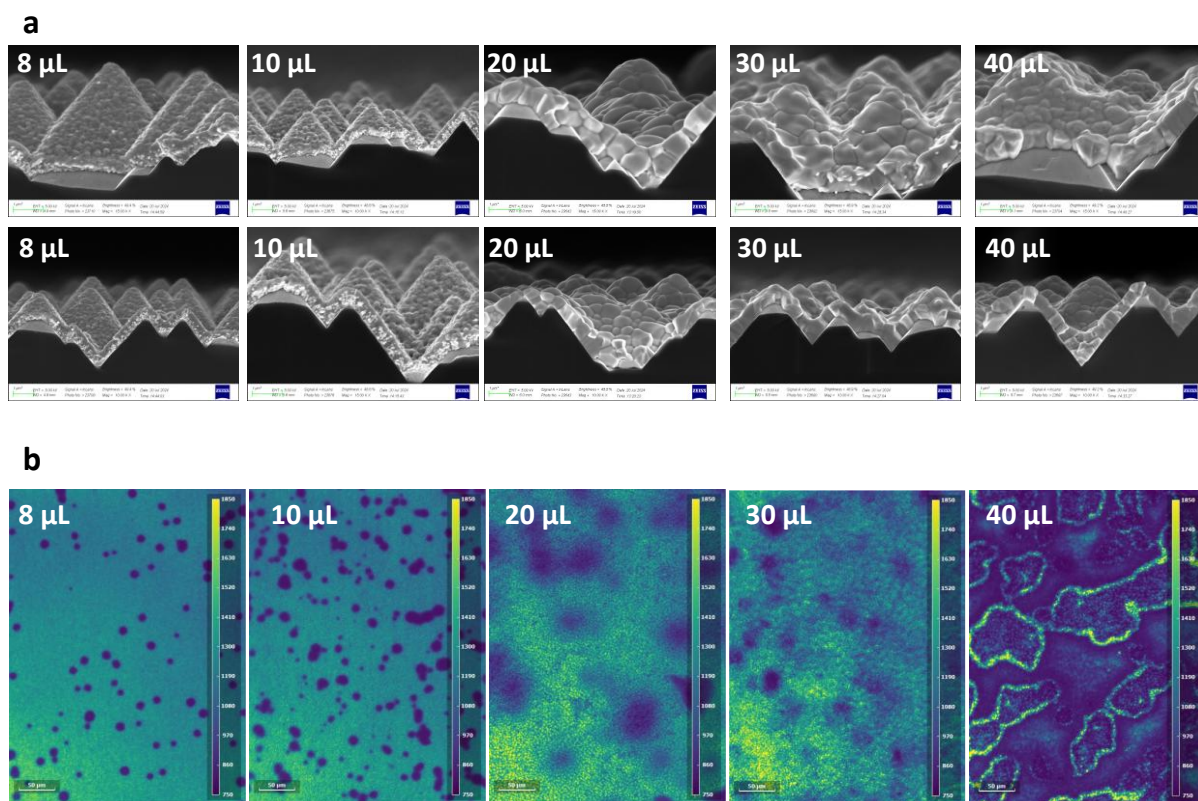


Figure S9. Impact of the solution volume on the perovskite's morphological and optoelectronic properties. (a) Cross-sectional SEM images, and (b) 2D PL intensity images taken at the peak energy 1.68 eV of perovskite films with a variation in solution volume (from hyperspectral PL measurements). With increased solution volume and up to an optimum of 20 μL the perovskite morphology is enhanced, and the optoelectronic response is improved.

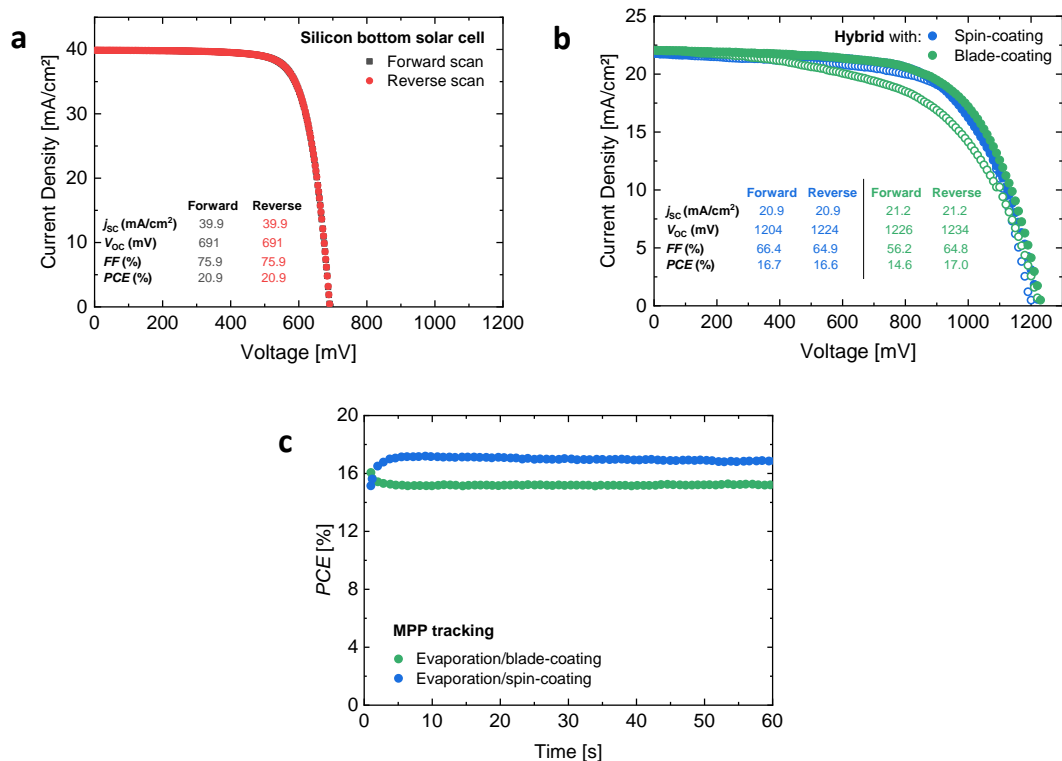


Figure S10. Single-junction solar cell performance. jV curve of (a) a silicon single-junction solar cell and (b) perovskite single-junction solar cells with hybrid evaporation/spin-coating and hybrid evaporation/blade-coating. The silicon solar cell uses non-optimized TCO and metal grid, limiting its performance. The cells are fabricated with an active area of ~ 1 cm², on ohmic textured silicon substrates. (c) MPP tracking of champion single-junction perovskite solar cells. After a stabilization period in the first 5 s, a stable output is obtained in both devices.

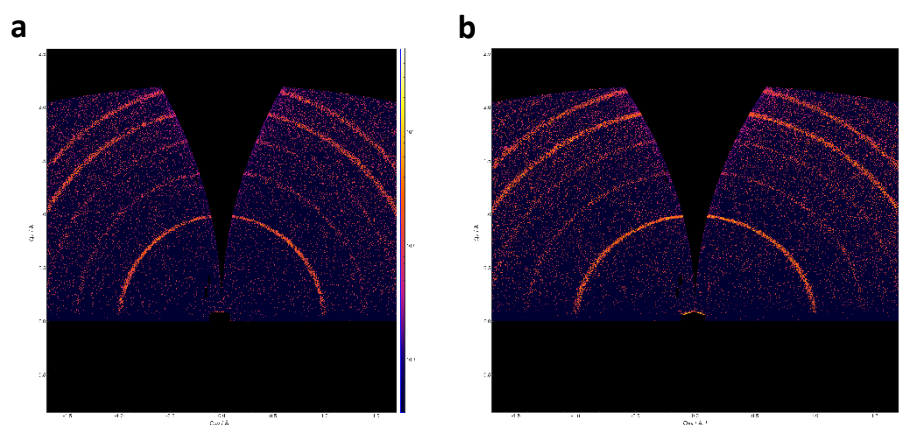


Figure S11. GIWAXS data of textured silicon/ITO/Me-4PACz/perovskite stacks where the perovskite film is fabricated with either (a) hybrid evaporation/spin-coating or (b) hybrid evaporation/blade-coating. A similar pattern is obtained for the perovskite films.

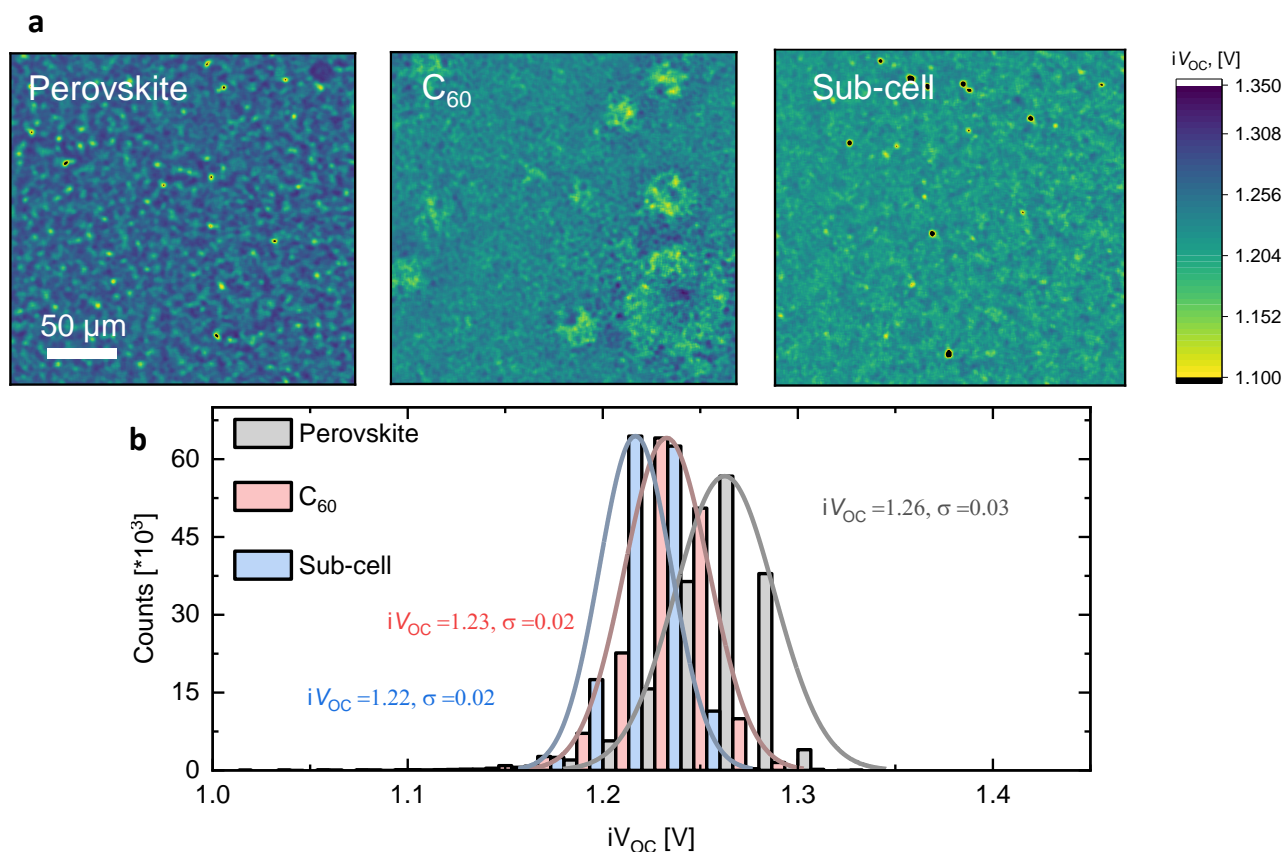


Figure S12: Analysis of non-radiative recombination losses in the perovskite sub-cell. (a) iV_{OC} images for different stacks. (b) Histogram of extracted iV_{OC} values. In the legend, Perovskite denotes textured silicon/ITO/Me-4PACz/perovskite/PDAI, C_{60} denotes textured silicon/ITO/Me-4PACz/perovskite/PDAI/ C_{60} , and sub-cell refers to measurements carried out on the whole tandem cell, where the chosen laser wavelength of 532 nm enabled top sub-cell excitation. The measurements were carried out in air on non-encapsulated samples. The perovskite half-stack shows an iV_{OC} of 1.26 V, which decreases to 1.23 V in the C_{60} stack, and further down to 1.22 V in the sub-cell. The measurements indicate a relatively low non-radiative recombination loss at the perovskite/ C_{60} interface and a high potential for voltage increase in the perovskite half-stack (e.g. through enhancing the HTL/perovskite interface and/or further improving the perovskite bulk). Note that the calculated value of the sub-cell can differ from one cell to the other (can be higher than 1.22 V since measured V_{OC} was found up to 1.23 V), and thus these values should be regarded with care.

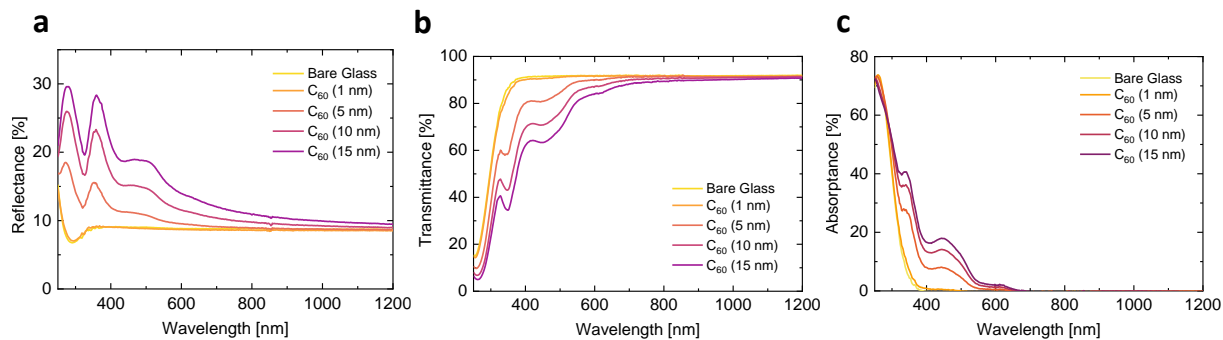


Figure S13: Analysis of parasitic absorption in C₆₀ as a function of its thickness. (a) Reflectance, (b) transmittance, and (c) absorptance data of C₆₀ layers with different thickness. The layers are deposited on top of a glass substrate. With decreasing thickness of C₆₀, the absorptance decreases.

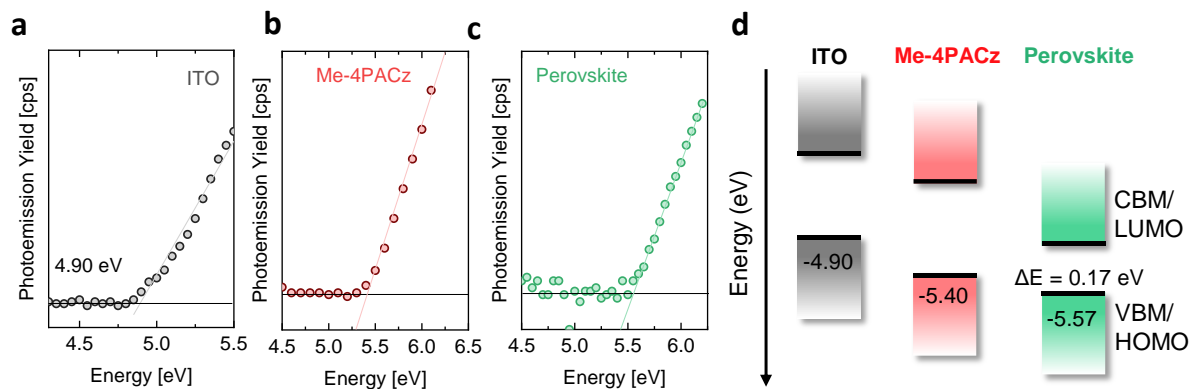


Figure S14: Analysis of energetic offset at the HTL/perovskite interface. PESA measurements on (a) bare ITO substrate, (b) textured silicon/ITO/Me-4PACz, and (c) textured silicon/ITO/Me-4PACz/perovskite. (d) Constructed energy band diagram. A high energy offset ΔE of 170 meV is observed between the perovskite's VBM and the HTL's HOMO, indicating further potential for FF and V_{OC} increase with e.g. buried interface engineering strategies.

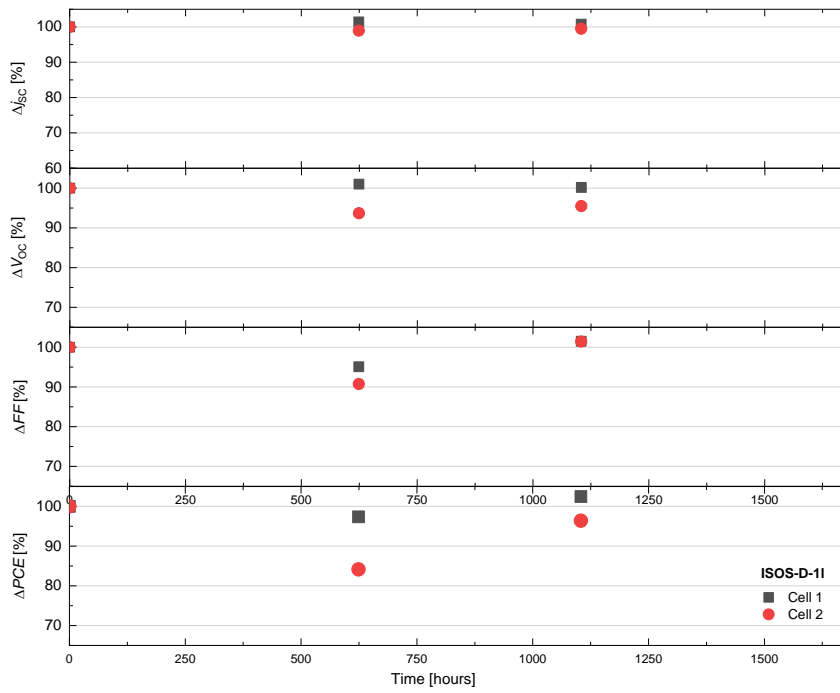


Figure S15: ISOS-D-11 stability testing of two tandem solar cells with the optimized perovskite in this work. The data from reverse scan is shown. Over the 1680 hour testing period, the cells are aged in the GB, in the dark, at room temperature, without electrical bias. The cells are taken at different instances for jV characterization in air. The devices retain 96.8% and 99.8% of their initial PCE by the end of the testing period.

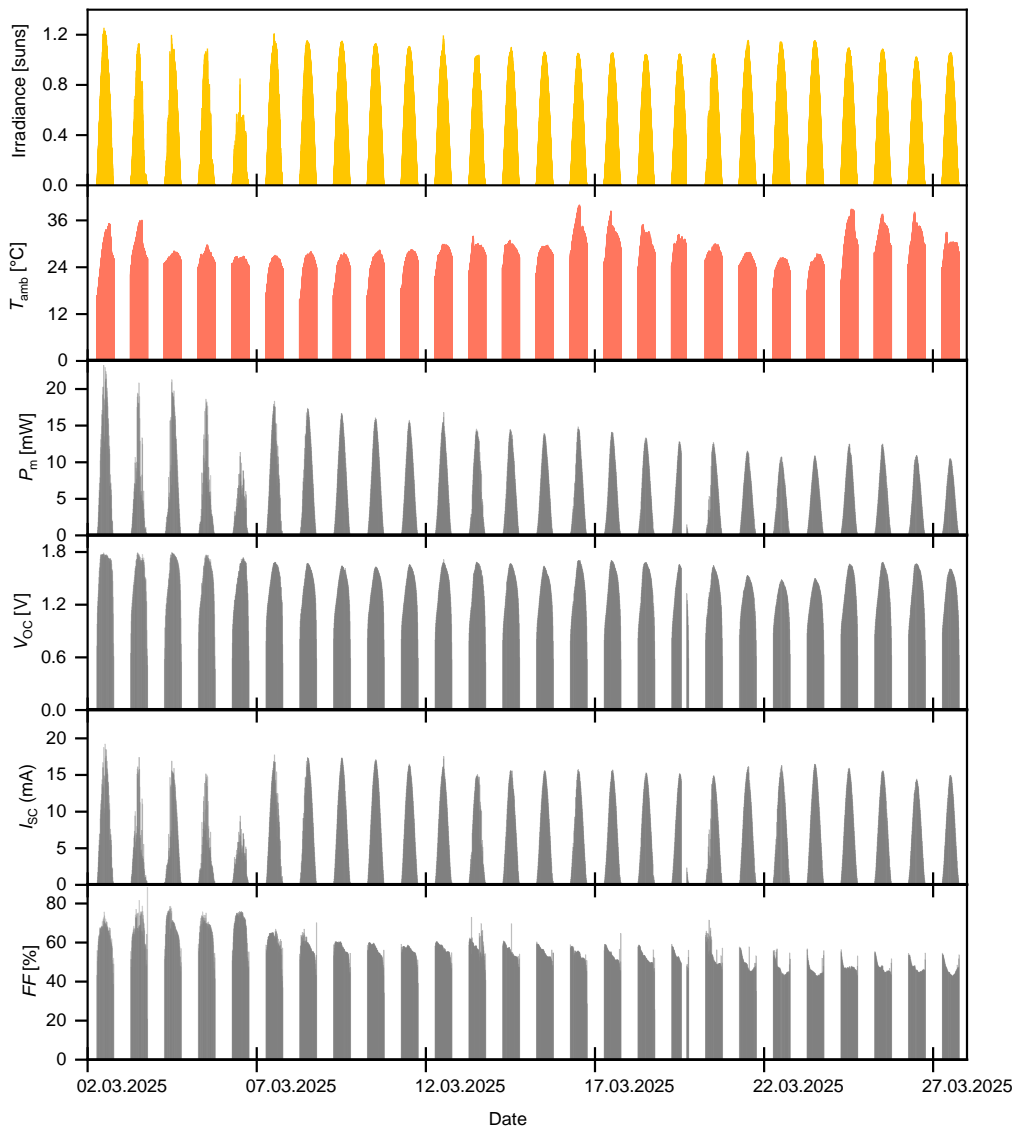


Figure S16: Outdoor stability testing of the optimized perovskite in this work. Over the one month testing period, the encapsulated cell (same cell that experienced ISOS-D-11 test in Figure S15) was aged at the Red Sea coast. This test encompassed all operational conditions, including continuous exposure to light and heat, as well as temperature fluctuations between day and night. Peak device temperatures reached up to 40°C, while light intensity on sunny days peaked at 1.26 suns (measured via pyranometer) around noon. The *PCE* of the device fell to 45% by the end of the testing period, mainly driven by degradation of *FF*.

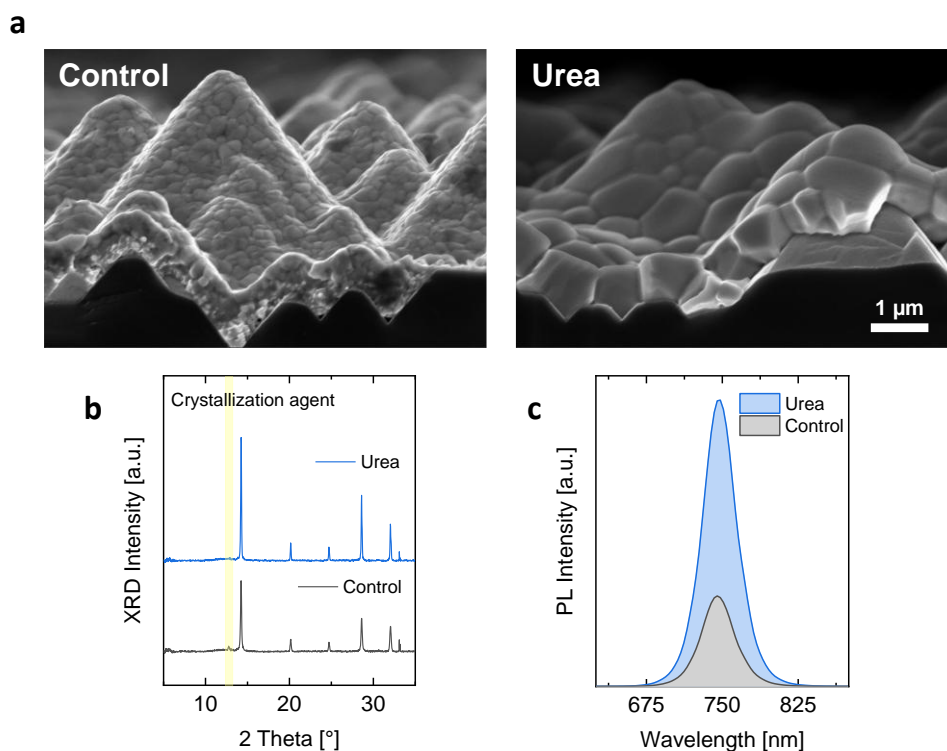


Figure S17: Impact of urea crystallization agent on the perovskite film properties with the hybrid evaporation/blade-coating method. (a) Cross-sectional SEM images, (b) XRD data and (c) PL spectra of perovskite films with and without the addition of urea as a crystallization agent (spectra averaged from area of $40\ \mu\text{m} \times 40\ \mu\text{m}$ from hyperspectral imaging). The control perovskite does not contain urea and is annealed at 150°C for 25 mins. Addition of urea enhances the perovskite film morphology, crystalline quality, and conversion rate. More broadly, it demonstrates that the use crystallization agents in the context of perovskite fabrication with the hybrid evaporation/blade-coating method is crucial to further enhance the perovskite film's quality.

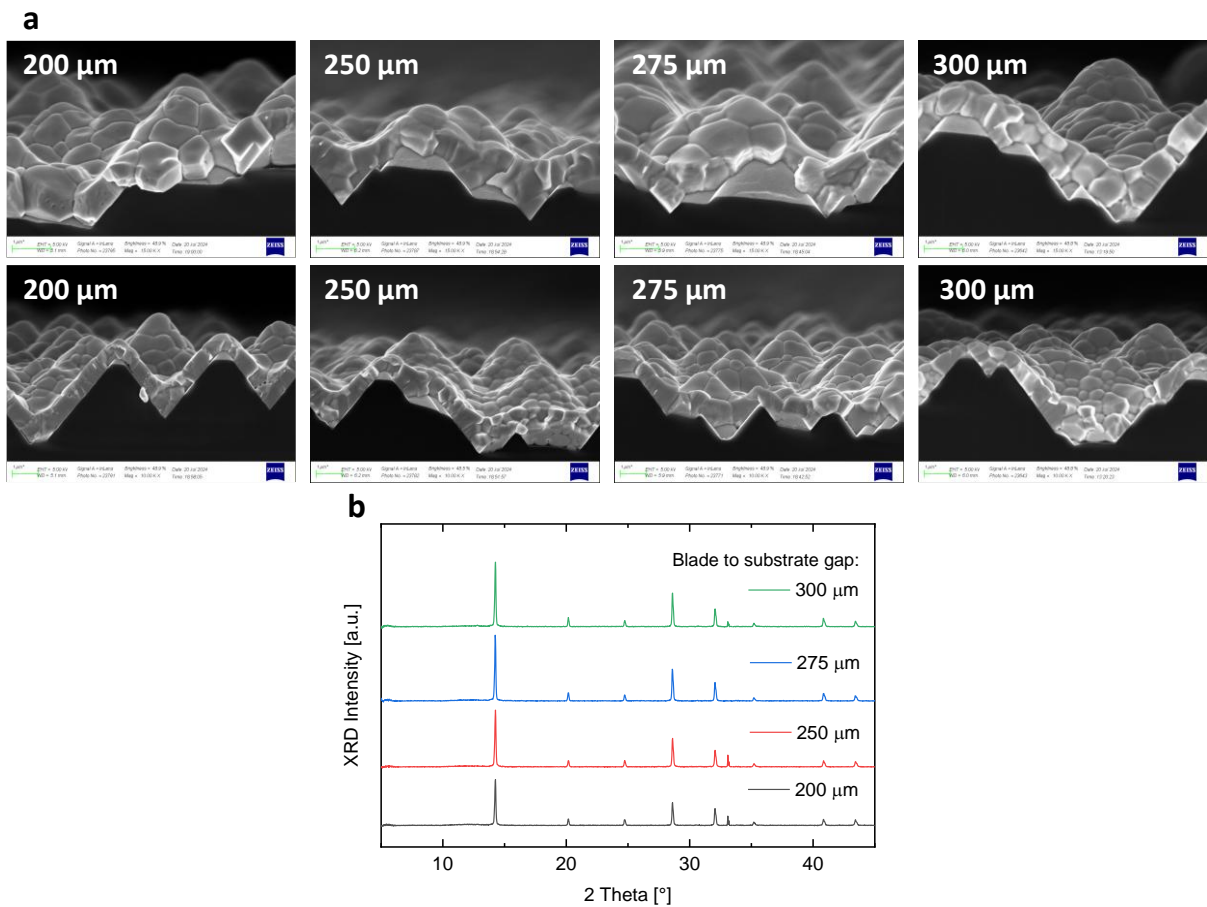


Figure S18. Impact of the blade gap on the perovskite's morphological and structural properties. (a) Cross-sectional SEM images, and (b) XRD data of perovskite films with a variation in blade gap. The impact of the blade gap in the tested range is minimal. However, we note that the blade gap should be controlled to (1) avoid damaging the substrate at low gap distances and (2) enable solution coating (beyond a certain value of the blade gap, the solution cannot be dragged across the substrate).

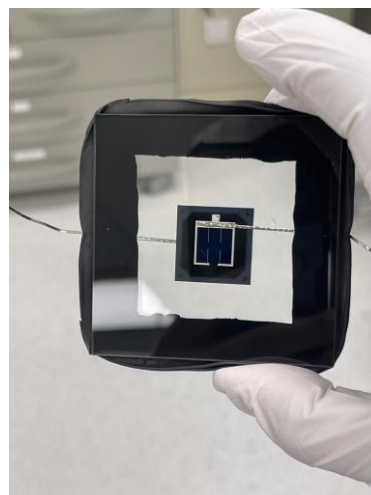


Figure S19. Photograph of the encapsulated cell.

Section 1: Darcy's law

Darcy's law is an equation that describes the flow of a fluid through a porous medium. It is shown below:

$$Q = \frac{kA}{\mu L} \Delta p$$

Q is the flux, k is the permeability, Δp is the pressure drop over a distance L and a cross-section A , and μ is the viscosity. The equation shows that fluids with a high viscosity reduce the flux Q .

Besides, one can note that Darcy's law indicates a further enhancement of the flux, which in our study can be interpreted as the solution's infiltration into the scaffold and thus the perovskite conversion rate, if e.g. the permeability k – which can be translated to the porosity of the scaffold – is increased, or the solute radius R_0 – which denotes the size of organohalide molecules – is reduced.

References

- 1 E. J. Cassella, E. L. K. Spooner, T. Thornber, M. E. O'Kane, T. E. Catley, J. E. Bishop, J. A. Smith, O. S. Game and D. G. Lidzey, *Adv. Sci.*, 2022, **9**, e2104848.
- 2 S. Mariotti, I. N. Rabehi, C. Zhang, X. Huo, J. Zhang, P. Ji, T. Wu, T. Li, S. Yuan, X. Liu, T. Guo, C. Ding, H. Wang, A. Bruno, L. K. Ono and Y. Qi, *Energy & Environ Materials*, 2025, **8**.
- 3 E. Parvazian, R. Garcia-Rodriguez, D. Beynon, M. L. Davies and T. Watson, *Slot-Die Coating of Self-Assembled Monolayers: A Scalable Approach for Perovskite Solar Cells*, 2025.
- 4 Shihao Yuan, Daming Zheng, Ting Zhang, Yafei Wang, Feng Qian, Lei Wang, Xiaobo Li, Hualin Zheng, Zecheng Diao, Peng Zhang, Thierry Pauporté and Shibin Li, *Scalable Preparation of Perovskite Films with Homogeneous Structure via Immobilizing Strategy for High-performance Solar Modules*, 2025.
- 5 B. Abdollahi Nejang, D. B. Ritzer, H. Hu, F. Schackmar, S. Moghadamzadeh, T. Feeney, R. Singh, F. Laufer, R. Schmagar, R. Azmi, M. Kaiser, T. Abzieher, S. Gharibzadeh, E. Ahlswede, U. Lemmer, B. S. Richards and U. W. Paetzold, *Nat Energy*, 2022, **7**, 620–630.
- 6 B. P. Kore, O. Er-raji, O. Fischer, A. Callies, O. Schultz-Wittmann, P. S. C. Schulze, M. Bivour, S. de Wolf, S. W. Glunz and J. Borchert, *Energy & Environmental Science*, 2024.
- 7 A. Farag, T. Feeney, I. M. Hossain, F. Schackmar, P. Fassel, K. Küster, R. Bäuerle, M. A. Ruiz-Preciado, M. Hentschel, D. B. Ritzer, A. Diercks, Y. Li, B. A. Nejang, F. Laufer, R. Singh, U. Starke and U. W. Paetzold, *Adv. Energy Mater.*, 2023, **13**.
- 8 O. Er-raji, M. A. Mahmoud, O. Fischer, A. J. Ramadan, D. Bogachuk, A. Reinholdt, A. Schmitt, B. P. Kore, T. W. Gries, A. Musiienko, O. Schultz-Wittmann, M. Bivour, M. Hermle, M. C. Schubert, J. Borchert, S. W. Glunz and P. S. Schulze, *Joule*, 2024, **8**, 2811–2833.
- 9 O. Er-raji, C. Messmer, R. R. Pradhan, O. Fischer, V. Hnapovskyyi, S. Kosar, M. Marengo, M. List, J. Faisst, J. P. Jurado, O. Matiash, H. Pasanen, A. Prasetio, B. Vishal, S. Zhumagali, A. R. Pininti, Y. Gupta, C. Baretzky, E. Ugur, C. E. Petoukhoff, M. Bivour, A. A. Said, E. Aydin, R. Azmi, J. Schön, F. Schindler, M. Schubert, U. Schwingenschlögl, F. Laquai, J. Borchert, P. S. C. Schulze, S. de Wolf and S. W. Glunz, *In peer review*, 2025.
- 10 A. Delamarrea, L. Lombez and J. F. Guillemoles, *Physics, Simulation, and Photonic Engineering of Photovoltaic Devices*, 2012, **8256**, 825614.